20th Australasian Fluid Mechanics Conference
Perth, Australia
5-8 December 2016

The impact of bathymetry on a laboratory-scale two-layer flow

Y. Yuan[1], Y. Lv[1], L.-T. Lin[1] and Z. He[1*]

[1]Ocean College, Zhejiang University, Hangzhou 310058, China

Abstract

The stratified flow over complex bathymetry has received great interest over recent decades. Many studies have applied the internal hydraulic control and maximal two-layer exchange theory to interpret the mixing and entrainment between two layers. However, the dynamical behavior of the simplest two-layer flow, a dense saline current intruded into quiescent uniform density ambient water with various bathymetries, is not yet fully understood. In this study, we designed a series of laboratory experiments to compare dense current flows over an obstacle, such as a sill at the river mouth. All experiments were carried out in a long flume over a range of density difference with various obstacle shape and height. Cross-section view of the dense current is visualized by potassium permanganate and the velocity field is measured with the Particle Imaginary Velocimetry (PIV) technique. The laboratory results will be compared with 2-1/2 layer flow theory and used to inform the field observation data at a narrow channel with complex bathymetry near Zhoushan, China.

Introduction

Gravity currents, also called dense currents, are driven by a density difference between two regions of fluid and play an important role in the exchange of materials between two fluids (Simpson, 1999). Much of our understanding of gravity currents is based on lock-exchange experiments under a flat bottom condition. A number of studies have examined the propagation of the gravity currents using lock-exchange laboratory experiments. When the gravity currents move along the flat-bottom in uniform density ambient water, the front velocity quickly rises to the maximum velocity and maintains a constant speed for at least six lock-lengths and then decreases due to the bottom friction (Nogueira et al., 2013). Huppert and Simpson (1980) divided this process into three phases, i.e., the slumping phase, inertial phase and viscous phase.

However, gravity currents in geophysical environments and engineering processes often encounter complicated bathymetries, such as a sill at the river mouth or a dyke in the reservoir. When gravity currents meet an obstacle, both in natural and man-made environment, only a portion of current would flow over the obstacle (Lane-Serff et al., 1995), or even be completely blocked if the obstacle higher than 2 times of the dense current height (De Ceasare et al., 2008).

To investigate the impacts of obstacles on gravity currents, a number of laboratory experiments have been conducted. For instance, Oshaghi et al. (2013; 2014) studied the effect of inlet Froude number on turbidity currents passing over an obstacle. Asghari Pari et al. (2010) investigated the effects of obstacle height on controlling turbidity current. Greenspan and Young (1978) did a series of experiments on gravity currents encountering different shape obstacles. They suggested that the shape of obstacle does not affect the gravity current propagation speed. Prinos (1999) conducted a series of experiments using triangle and semi-circular shaped obstacle and found the similar conclusion.

In the present study, the advanced measurement technique allows detailed analysis of gravity current velocity field around the obstacle. The manuscript is organized as follows. In section 2, we describe the experimental setup and two main measurement approaches. We present the experimental results of influence on propagation speed and energy under different conditions in section 3. Our conclusions are summarized in section 4.

Experiment methods

A schematic of the lock-exchange experiment is shown in Figure 1. All experiments were conducted in a rectangular tank of 200 cm long, 20 cm wide, and 20 cm deep. The head tank with length of 9.5 cm was separated from the rest of tank by the lock. In all experiments, ambient fresh water and dense saline water were filled to two sides of the lock simultaneously until the water level on both sides reached to 19 cm. The obstacle with different shape and height was placed at 47.5 cm downstream of the lock (i.e., 5 times of the head tank length). The distance between the obstacle and lock ensure the gravity current reaches the obstacle during the steady phase (Gonzalerz-Juez and Meiburg, 2009). To initiate the experiment, the electric gate was removed rapidly and smoothly to minimize the possible disturbance.

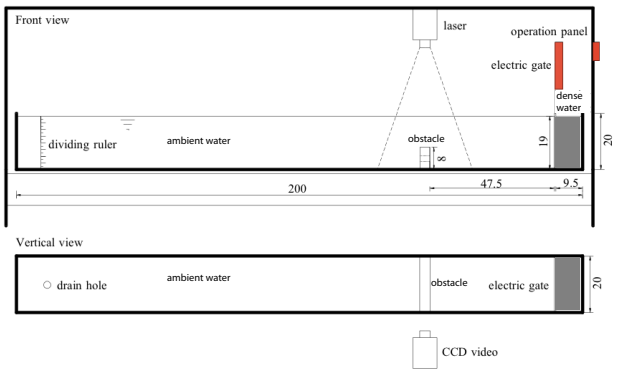

Figure 1. Side view (upper) and plan view (lower) of the channel used in the experiments for gravity currents meeting the obstacle. The ambient is filled with fresh water, and dense saline water is confined in the lock region (dark gray region). All measurements are in cm.

In the qualitative experiment, the dense saline water was dyed with potassium permanganate (Dai, 2013). A digital camcorder with resolution of 4928 pixel × 3264 pixel at a frame rate of 25 fps was placed on the side of the water tank to obtain the overall view of flow motion. In the quantitative experiment, we investigated the detailed velocity field and mixing processes of dense saline current using an advanced Particle Image Velocimetry (PIV) technique. A MGL-N-532 continuous wave laser was mounted on top of the obstacle to create a laser sheet at the study region, which is about 30 cm x 22 cm. The PIV images were captured by charge-couple device (CCD) camera with a resolution of 2320 pixel × 1726 pixel at a frame rate of 200 fps.

The velocity field was calculated using a pair of two images with short time interval by PIVLab software (Thielicke and Stamhuis, 2014).

Sixteen lock-exchange experiments were conducted in the water tank at different saline water density, obstacle shape and height. Experimental parameters for all runs are provided in Table 1. In all experiments, the gravity current is under subcritical condition as the inflow Froude number ($Fr_0 = U/\sqrt{g_0' H_0}$) (Benjamin, 1968) is less than one, where U is the average front speed during the experiment, $g_0' = \frac{\rho_a - \rho_c}{\rho_a} g$ is the reduced gravity between two fluids, ρ_a is the density of ambient water, ρ_c is the density of the saline water and H_0 is the total water depth. There is no obstacle in run 1 – 4, which are used as the control experiments. Triangle and square obstacles with different height are used in run 5 - 10 and 11 - 16, respectively. Runs with higher density difference (i.e., higher reduced gravity g_0') were repeated for the PIV measurements. The inflow Reynolds number $Re_0 = UH_0/\nu$ (ν is the kinematic viscosity) is always larger than 1000 (Dai, 2013), indicating that the viscous effect can be ignored.

Run	Obstacle shape	h_b (cm)	ρ_c (kg/m³)	g_0' (m/s²)	Re_0	Fr_0
1	N.A	0	1011.4	0.112	10564	0.381
2	N.A	0	1012.8	0.125	12103	0.413
3	N.A	0	1022.7	0.222	15010	0.385
4	N.A	0	1023.9	0.234	15732	0.393
5	Triangle	3	1012.8	0.125	11172	0.382
6	Triangle	3	1023.9	0.234	14725	0.368
7	Triangle	5	1012.8	0.125	10336	0.353
8	Triangle	5	1023.9	0.234	12654	0.316
9	Triangle	8	1012.8	0.125	8322	0.284
10	Triangle	8	1023.9	0.234	11381	0.284
11	Square	3	1011.4	0.112	10678	0.385
12	Square	3	1022.7	0.222	12749	0.327
13	Square	5	1011.4	0.112	9975	0.360
14	Square	5	1022.7	0.222	12141	0.311
15	Square	8	1011.4	0.112	6973	0.252
16	Square	8	1022.7	0.222	9386	0.241

Table 1. The parameters of the experiments.

Results

Dense current evolution

When the lock was lifted up quickly, dense saline fluid propagated underneath of the fresher ambient water. Figure 2 compares the evolution of gravity current propagating into uniform-density ambient water without and with an obstacle. Without the obstacle, the development of dense current shows three distinct phases, namely, the acceleration phase, steady-state phase and deceleration phase (Figure 2a-c; Lane-Serff, et al., 1995). When an obstacle placed at the steady-state phase, the dense current never reaches the condition with constant front speed. Instead, the dense current decelerates before it meets the obstacle as a clear upward climbing can be observed during the experiment (Figure 2e). Subsequently, the dense current climbs down once after it passes the obstacle, and wraps around the obstacle (Figure 2f). Finally, the dense current reaches its second deceleration phase when it moves far away from the obstacle (Figure 2g). The detailed definition of each phase will be presented in the following section using frontal propagation speeds.

Before the dense current meets the obstacle, it has a classical semi-ellipse shaped head followed by a thin tail. Due to the viscous effects on the bottom boundary, a slightly 'raised' nose can be observed in the experiment (Figure 2d). This is similar to the no obstacle case (Figure 2a-c) and previous research (Beghin et al., 1981; Dai, 2013). Once the dense current encounters the obstacle, it clearly lifts up and jumps the obstacle tip (Figure 2e). The slope of the gravity head front increases significantly right after it passes the obstacle, while the tail is thicker because the presence of the obstacle (Figure 2f). As the dense current moves further downstream of the obstacle, the semi-ellipse shaped head is formed again followed by a relatively thin tail (Figure 2g). At this phase, there is no clear difference in cases with and without the obstacle.

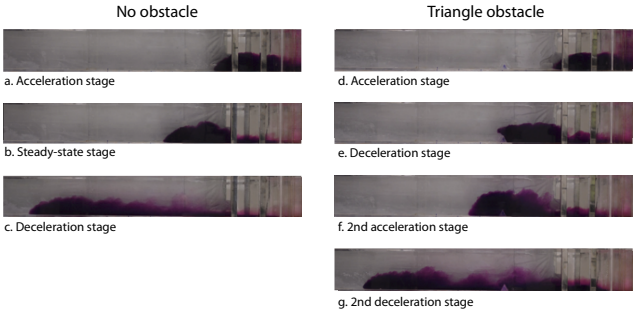

Figure 2. Color image series for the gravity current lock exchange experiment (left; run 4) and the same condition when gravity current meeting a 3 cm triangle obstacle (right; run 6).

Figure 3 shows several snapshots from PIV experiment with (a - d) and without (e - f) the obstacle. Enhanced vorticity at the interface can be observed in all experiment, indicating typical Kelvin-Helmholtz instabilities generated by the velocity shear. It is clear that the lower region of the dense current climbs up the obstacle, while the upper region is blocked by the obstacle and reflected backward. This is consistent with the analysis by Lane-Serff et al. (1995) that only portion of the gravity current flows over the obstacle. More importantly, the result suggests that the lower region of the gravity current has preference to flow over the obstacle. As the dense current passes the obstacle, the fluid jumps across and wraps around the obstacle. There is always a region of high vorticity downstream of the triangle obstacle tip.

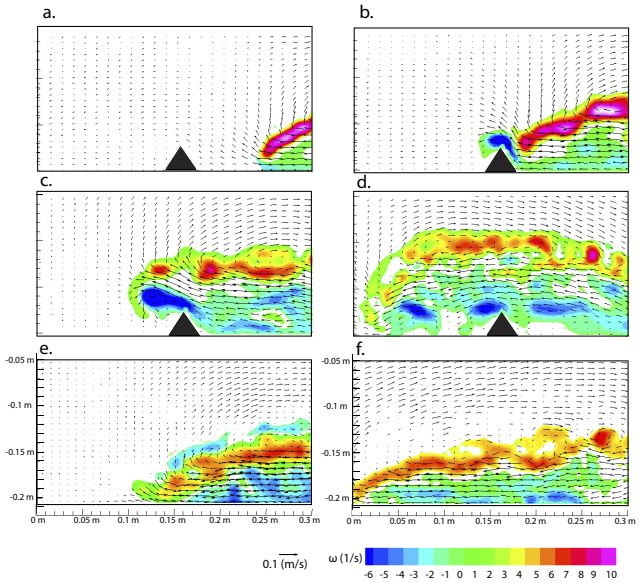

Figure 3. Typical PIV experiment results showing velocity fields (arrows) overlaid on vorticity fields (color). Panel a-d shows gravity current before, at, after, and away from a 3 cm triangle obstacle, similar to Figure

2 d-g. Panel e-f shows the same condition of panel c-d but with no obstacle.

Influence on front location and propagation speed

In this subsection, front location and frontal propagation speed under different experimental conditions are compared. Front location was measured as the nose of the dense current from color image series (Figure 1). The dense current frontal propagation speeds were normalized by the inflow internal wave speed, $c_0 = \sqrt{g_0' H_0}$. Figure 4 shows that the dense current starts to decelerate as it approaches the obstacle, and accelerate again once it passes the obstacle. As the obstacle height increasing, the force that the dense current needs to overcome in order to pass the obstacle increases. As the result, the dense current has a relatively smaller minimum speed at the end of the deceleration phase. Similarly, the second maximum speed that the current reaches at the end of the second acceleration phase is also smaller with a higher obstacle height.

Figure 4 shows the definition of each phase using the current propagation speed. In the no obstacle case, the front velocity quickly rises to the maximum velocity (U_{max} = $0.43c_0$) and maintains a constant speed for at least six lock-lengths and then decreases due to the bottom friction (Nogueira et al. 2013). The normalized maximum velocity is slightly smaller than the theoretical value of 0.5 predicted using energy-conserving theory by Benjamin (1968) and previous laboratory result of 0.48 by Shin, et al. (2004). Three phases are also defined as the slumping phase (Pn1 in Figure 4c), inertial phase (Pn3) and viscous phase (Pn3) by their controlling forces in Huppert and Simpson (1980). When an obstacle placed in the inertial phase, Lane-Serff et al. (1995) suggested that the flow might be divided into four regions: the inflow conditions (slumping phase; Po1), the region around the hydraulic jump (deceleration phase; Po2), the flow at the obstacle (acceleration phase; Po3) and the flow downstream of obstacle (viscous phase; Po4). The maximum propagation speed (U_{max}) is achieved at the end of the slumping phase. Upstream of the obstacle, dense current decelerates because kinetic energy transferred into potential energy through the hydraulic jump and it reaches to its minimum speed (U_{min}) at the end of the this phase. Once the current passes the obstacle it accelerates again as the potential energy is converted back to kinectic energy. The difference between the second maximum speed (2^{nd} U_{max}) after this phase and the U_{max} indicates the energy dissipated during the current passes the obstacle. It is possible that enhanced mixing in the wake of the obstacle results in a reduction of 2^{nd} U_{max}.

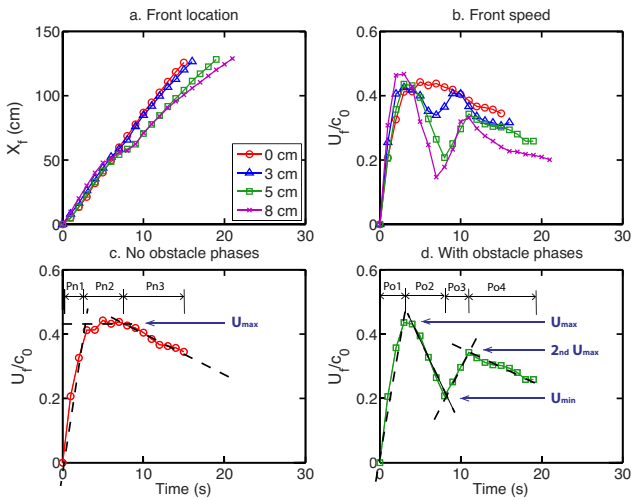

Figure 4. The front location (a) and normalized frontal propagation speed (b) against time for gravity current meeting a triangle obstacle with different height. The definitions of velocity extremes (U_{max}, 2^{nd} U_{max}, U_{min}) and phases (Pn1-3; Po1-4) are shown in panel c and d for runs without and with the obstacle, respectively.

Figure 5 shows the front location and propagation speed with different inflow density difference and obstacle shape. There is no significant difference in the front location and propagation speed with triangle (inclination angle = 60^o – 80^o) and square (inclination angle = 90^o) shaped obstacle. This is consistent with the previous research by Greenspan and Young (1978) and Prinos (1999). They both suggested that the dependence of the inclination of the obstacle is relatively small using theoretical analysis and laboratory simulation. Without the obstacle the normalized propagation speeds with different inflow reduced gravity collapse (Figure 5c). However, the influence of obstacle is dramatically different with different inflow reduced gravity (Figure 5d). With higher reduced gravity, the dense current reaches to its third and forth phase earlier, presumably due to the higher internal wave speed in these cases. Higher reduced gravity also leads to a lower U_{min} and 2^{nd} U_{max}, although the maximum propagation speed is almost the same in all cases. The normalized propagation speed in the viscous phase is always smaller in cases with the higher reduced gravity.

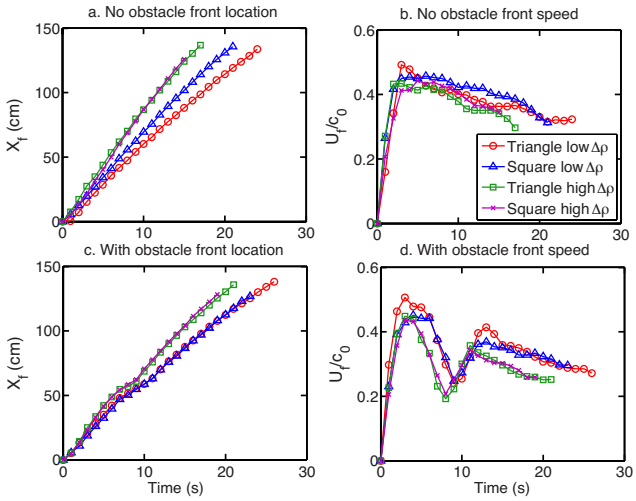

Figure 5. The front location and normalized frontal propagation speed against time for gravity currents meeting a 5 cm obstacle with different shape and reduced gravity (c and d). The same condition with no obstacle are plotted in panel a and b for comparison.

In figure 6, we quantify the maximum and minimum propagation speeds and acceleration rate in all cases. The acceleration rate is calculated by the least-square linear fit in each phase (Figure 4c and 4d). It needs to point out that there is no minimum velocity, 2^{nd} maximum velocity, 2^{nd} phase and 3^{rd} phase in no obstacle cases (obstacle height = 0cm). The normalized maximum speed is in the range of 0.4 – 0.5, consistent with the classical theory (Benjamin, 1968; Barr, 1967). The dense current reaches to its minimum speed when the most of the kinetic energy transferred to the potential energy as it climbs up the obstacle. As a result, the minimum speed is smaller as the obstacle height increases. The difference between the maximum speed and 2^{nd} maximum speed represents the energy loss when the dense current meets the obstacle. The higher the obstacle is, more energy will be dissipated (i.e., larger difference between two speeds) when the dense current flows across the obstacle. The acceleration rate in the first phase and last phase is dominated by the density difference between two fluids and the viscous at the lower boundary, respectively. Both are independent with the obstacle height. However, the dynamics in the second and third phases are

controlled by the obstacle height. With higher obstacle height, the dense current has larger deceleration rate before the obstacle and larger acceleration rate after the obstacle. There is no significant difference with different obstacle shape in propagation speed and acceleration rate.

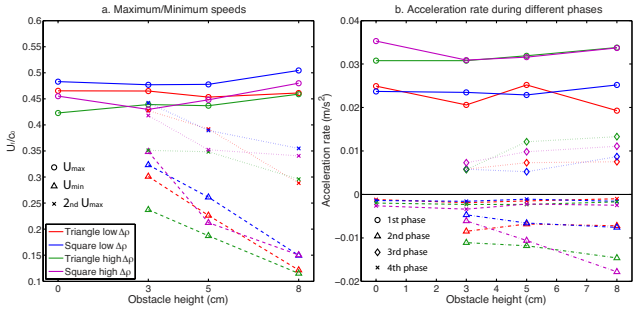

Figure 6. Normalized frontal propagation speed extremes (a) and acceleration rates (b) against obstacle height during different phases. Definitions of each parameter were discussed in Figure 4. Negative acceleration rate in 2nd and 4th phases indicates the gravity current is decelerating during these phases.

Conclusions

In this study, a series of lock-exchange experiments were conducted to investigate the gravity current propagation characteristics when it meets an obstacle. When an obstacle placed at the channel, the gravity current propagation reveals four phases, namely, the slumping phase, deceleration phase, acceleration phase, and viscous phase. The maximum propagation speed is achieved at the end of the slumping phase, in the range of 0.4 – 0.5 of the internal wave speed. This speed extreme is independent with the obstacle shape or height. The dense current propagation during the second and third phases is mainly controlled by the obstacle height and reduced gravity, while the impact of the obstacle shape is relatively small. With a higher obstacle height or a higher reduced gravity, the gravity current has a larger acceleration and deceleration rate during two phases. The energy is dissipated through the hydraulic jump before the obstacle. Therefore the propagation speed during the last three phases is always smaller with higher obstacle height.

Results from PIV experiments suggest that the lower portion of the dense current flows over the obstacle while the upper region fluid is blocked and reflects backward. More analysis on the PIV results is currently under investigating in order to understand the dynamics of the gravity current meeting the obstacle. Moreover, the mixing between two fluids and entrainment of the ambient water need to be further investigated in future by combining the Planer Laser-Induced Fluorescence (PLIF) technique to the present experiments.

Acknowledgments

This work was partially supported by the National Natural Science Foundation of China (No. 41506101) and Natural Science Foundation of Zhejiang Province (No. LQ14D060005).

References

[1] Asghari Pari, S. S, Kashefipour, S. M., Ghomeshi, M. & Bajestan, M. S., Effects of obstacle heights on controlling turbidity currents with different concentrations and discharges, *Journal of Food, Agriculture and Environment,* 8(2), 2010, 930-935.

[2] Barr, D. I. H., Densimetric exchange flows in rectangular channels. La Houille Blanche 22, 1967, 619–631.

[3] Beghin, P., Hopfinger, E. J., & Britter, R. E., Gravitational convection from instantaneous sources on inclined boundaries. *J. Fluid Mech.*, 107(1), 1981, 407-422.

[4] Benjamin, T. B., Gravity currents and related phenomena. *J. Fluid Mech.*, 31(02), 1968, 209-248.

[5] Dai, A., Experiments on gravity currents propagating on different bottom slopes, *J. Fluid Mech.,* 731, 2013, 117-141.

[6] De Cesare, G., Oehy, C.D., & Schleiss, A.J., Experiments on turbidity currents influenced by solid and permeable obstacles and water jet screens, in *6th International Symposium on Ultrasonic Doppler Methods for Fluid Mechanics and Fluid Engineering,* 2008.

[7] Gonzalez-Juez, E. & Meiburg, E., Shallow-water analysis of gravity-current flows past isolated obstacles, *J. Fluid Mech.*, 635, 2009, 415-438

[8] Greenspan, H. P. & Young, R. E., Flow over a containment dyke. *J. Fluid Mech.* 87(1), 1978, 179-192.

[9] Huppert, H. E., & Simpson, J. E., The slumping of gravity currents, *J. Fluid Mech.*, 99(04), 1980, 785-799.

[10] Lane-Serff, G. F., Beal, L. M. & Hadfield, T. D., Gravity current flow over obstacles. *J. Fluid Mech.* 292, 1995, 39-53.

[11] Nogueira, H. I., Adduce, C., Alves, E., & Franca, M. J., Analysis of lock-exchange gravity currents over smooth and rough beds, *J. Hydraul. Res.*, 51(4), 2013, 417-431.

[12] Oshaghi, M.R., Afshin, H., & Firoozabadi, B., Experimental investigation of the effect of obstacles on the behavior of turbidity currents. Canadian Journal of Civil Engineering, 40(4), 2003, 343–352.

[13] Prinos, P. 1999, Two-dimensional density currents over obstacles. *Proc. 28th IAHR Congress (CD-ROM)*, Graz, Austria, Theme D.

[14] Shin, J. O., Dalziel, S. B., & Linden, P. F., Gravity currents produced by lock exchange. *J. Fluid Mech.*, 521, 2004, 1–34.

[15] Simpson, J. E., *Gravity currents: In the environment and the laboratory*, Cambridge University Press, Cambridge, 1999.

[16] Thielicke, W., & Stamhuis, E. J, PIVlab-Towards user-friendly, affordable and accurate digital particle image velocimetry in MATLAB, *J. Open Res. Softw.*, 2(1), 2014, e30.